Chemical Engineering Journal 451 (2023) 138943

Contents lists available at ScienceDirect

Chemical Engineering Journal

journal homepage: www.elsevier.com/locate/cej

K^+ and CeO_2 nanoparticles modified OMS-2 nanorods for enhanced activity and stability of photocatalytic toluene oxidation: K^+ charge modulation and mechanistic investigation

Pingping Yu [a], Nan Li [a], Weixin Zou [a,b,*], Xiaoqian Wei [a], Jiawei Ji [a], Li Han [a], Yandi Cai [a], Wei Tan [a], Bin Gao [c], Lin Dong [a,b]

[a] School of Chemistry and Chemical Engineering, State Key Laboratory of Pollution Control and Resource Reuse, School of the Environment, Nanjing University, Nanjing 210023, PR China
[b] Jiangsu Key Laboratory of Vehicle Emissions Control, Center of Modern Analysis, Nanjing University, Nanjing 210023, PR China
[c] Department of Agricultural and Biological Engineering, University of Florida, Gainesville, FL 32611, United States

ARTICLE INFO

Keywords:
K^+ ion
CeO_2/MnO_2
Photocatalytic toluene oxidation
Charge modulation
Adsorbed oxygen species

ABSTRACT

For photocatalytic toluene oxidation, available photo-generated charges and active oxygen species are of great importance. Due to the advantages of K^+ and CeO_2, CeO_2/K-OMS-2 (Ce/KM) were prepared for photocatalytic toluene oxidation, which exhibited better activity and stability than that of Ce/0M (no K^+) and K-OMS-2. The band structures and DFT calculations revealed that K^+ in the K-OMS-2 tunnels changing Fermi levels led to Z-scheme heterojunction formation, and acting as charge modulation kinetically promoted photo-charge transfer. Meanwhile, the charge balance of K^+ increased the proportion of Mn^{3+}, leading to the generation of hydroxyl groups for toluene adsorption via strong OH-π interactions. In addition, oxygen adsorbed on Ce^{3+} and □-Ce^{3+}-O-Ce^{4+}, and enhanced oxygen migration were observed on Ce/KM, which further interacted with photo-generated charges to generate radicals. *In situ* DRIFTS and GC–MS suggested the degradation pathway, *i.e.*, the oxidizing radicals on Ce/KM attacked methyl of toluene, formed benzaldehyde, benzoic acid intermediates, opened benzene ring and finally mineralized into carbon dioxide and water. Notably, benzyl alcohol intermediate deposited and poisoned only K-OMS-2, not Ce/KM, confirming the excellent stability of Ce/KM. Furthermore, the effects of the humidity on reaction process were revealed.

1. Introduction

Under the circumstance of maintaining the earth's ecological environment, indoor volatile organic compounds (VOCs) emitted from oil plants, construction/decorative materials are considered as the vital target to be eliminated [1,2]. As one of the most significant pollutants of VOCs, it is vitally necessary to degrade toluene which can cause health disorders including headache, memory impairment and so on. Various disposal methods have been developed for air pollution remediation, such as adsorption, photocatalytic oxidation and catalytic combustion [3–6]. Among this disposal technologies, heterogeneous photocatalytic oxidation is deemed to the most attractive technology for its advantages in cost-effectiveness, conversion efficiency as well as mild operating conditions, which can directly convert organic compounds to CO_2 and H_2O. For photocatalytic toluene oxidation, the toluene adsorption on photocatalyst surface is the prerequisite. The toluene molecule was provided with the benzene ring with rich π electrons, which are facilitated to adsorb on the electron-deficient sites (e.g. OH and O_v) of photocatalysts [7–9]. Furthermore, the reaction products and pathways were complex, and benzyl alcohol, benzaldehyde, benzoic acid, and some ring-opening intermediates were reported [10–12]. It was suggested that the opening ring was of great importance to deep oxidation and pollutant mineralization [13–15].

The transition metal oxide photocatalysts (e.g. ZnO, TiO_2, ZrO_2, SnO_2, WO_3, MnO_2 and Fe_2O_3) are deeply studied as the most promising materials against indoor air pollutants with rapidly growing applications [5], due to inexpensive with excellent catalytic ability, various oxidation states and superior redox performance [16]. The reason why

* Corresponding author at: School of Chemistry and Chemical Engineering, State Key Laboratory of Pollution Control and Resource Reuse, School of the Environment, Nanjing University, Nanjing 210023, PR China.
E-mail address: wxzou2016@nju.edu.cn (W. Zou).

https://doi.org/10.1016/j.cej.2022.138943
Received 29 June 2022; Received in revised form 15 August 2022; Accepted 28 August 2022
Available online 1 September 2022

Mn-based catalysts are considered as promising photocatalysts, which are not only for the valance controllability, but also for the excellent redox ability and oxygen storage activity [17,18]. Manganese oxides of various crystal forms including MnO, Mn_3O_4, Mn_2O_3 and MnO_2, owing to its environmental friendliness and high oxygen species adsorption, exhibit excellent potential in photocatalytic oxidation of VOCs such as formaldehyde, ethanol, benzene, toluene, phenol and benzyl alcohols [18–29]. Nanostructured cryptomelane-type manganese oxide octahedral molecular sieves (K-OMS-2) belongs to α-MnO_2, the K^+ in tunnel of which is beneficial to form K-O*(*OH)-Mn moieties and generate additional surface hydroxyl groups, increase the oxygen vacancy defects, improve the lattice oxygen mobility and performance in VOC abatement [30–32]. Wu *et al.* detected the effect of K^+ loading amount in OMS-2 and drew the conclusion that the promoted performance in toluene plasma-catalytic oxidization was owning to the more surface active oxygen species, abundant oxygen vacancies and more superior low-temperature reducibility [33]. It was already reported in literature that compared to OMS-2 without K^+ in tunnel (0-OMS-2), the K^+ modified OMS-2 could weaken Mn-O bonds, influence the thermal stability and chemical composition, form more surface active oxygen species and oxygen vacancies, which were facilitated to photocatalytic oxidation of toluene [33–35]. However, the role of K^+ modified OMS-2 in the migration direction of photogenerated charge lacks attention.

Proper structure construction is conducive to taking full advantage of the narrow band gap of manganese oxide to achieve better light absorption and photo-generated electron-hole pair separation [36,37]. A large number of studies have proved that constructing heterojunction, doping and surface modification by transition metals of OMS-2 can improve its physicochemical properties and catalytic activity [38]. Ye *et al.* prepared hierarchically porous α-MnO_2/Mn_3O_4 nanostructure and proved the formation of numerous intimate interfaces and a direct Z-scheme junction, which were facilitated to the increase of superoxide radicals and oxygen vacancies [39]. Semiconductor cerium oxide (CeO_2) have attracted numerous researches in the aspect of eliminating VOCs, such as the oxidation of formaldehyde, benzene, toluene and phenol [18,23,25,28]. As a rare earth element, Ce can alternate Ce^{3+} with Ce^{4+} flexibly as an excellent redox pair [40–42]. Its oxygen vacancy defects which can form and eliminate quickly contribute to the excellent oxygen storage capacity [43–45]. The abundant oxygen vacancies and oxygen storage capacity of CeO_2 were in favor of improving the oxygen mobility and redox ability in photocatalytic reaction [46]. Therefore, MnO_2-CeO_2 composites have been used in the photocatalytic toluene oxidation. For example, Ye and Ioannides *et al.* have proved that MnO_2-CeO_2 mixed oxides exhibit better activity and stability than individual metal oxides catalyst [47–50]. Zhao *et al.* successfully constructed $CeMn_xO_y$/OMS-2 nanocomposites and achieved an enhancement in the photo-thermocatalytic activity of benzene with UV–vis infrared irradiation [51]. That catalysts performed very excellent durability. At the heterostructures interface, MnO_2 and CeO_2 can generate the favorable synergistic effect that might be the key to improve the physicochemical properties [49]. In the work of Zhang *et al.*, a range of MnO_2(*x*)-CeO_2 oxides was synthesized for HCHO removal. Through the synergistic effects of MnO_2(*x*)-CeO_2, the lattice oxygen transferred to adsorbed oxygen and the catalytic activity was enhanced. Based on the fact that Ce element belonging to lanthanide elements has unique 4f orbit electrons, which are localized tightly near Fermi level or itinerant [38]. When modifying CeO_2 on OMS-2, the high density of f-electrons would interact with the Mn and K ions, influencing the electron structure and furthermore improve the photocatalytic activity of VOCs.

Therefore, in this work, CeO_2 nanoparticles were loaded on K-OMS-2 nanorods and employed to enhance the deep-oxidation of toluene of VOCs and inhibit photocatalyst deactivation. The performance of photocatalytic toluene degradation showed that with the help of CeO_2, the conversion of toluene to CO_2 was greatly improved. The important factors of active radicals were determined by *in-situ* ESR, and the band structures, interfacial electronic effects, and surface active oxygen species were investigated to reveal the different active radical generation through DFT calculations, VB-XPS and Mott-Schottky (M-S), O_2-TPD, and O1s XPS. Furthermore, *in situ* DRIFTS of toluene and H_2O adsorption under light irradiation and GC–MS results were employed to propose the possible reaction mechanism of photocatalytic toluene oxidation on Ce/KM nanorods, as well as the anti-deactivation process. The work would provide efficient ways to improve the Mn-based catalyst stability of photocatalytic toluene oxidation.

2. Experimental

2.1. Materials

Cerium nitrate hexahydrate ($Ce(NO_3)_3{\cdot}6H_2O$) and Potassium permanganate ($KMnO_4$) were purchased from Sinopharm Chemical Reagent Co., ltd., and Xilong Scientific Co., ltd. Maganese sulfate monohydrate ($MnSO_4{\cdot}H_2O$) and Ammonium sulfate ($(NH_4)_2SO_4$) were purchased from Nanjing Chemical reagent CO., ltd. Ammonium persulphate ($(NH_4)_2S_2O_8$) and Acetic acid (HAc) were obtained from Shanghai Hushi Laboratorial Equipment Co., ltd. All the chemicals were used directly of analytical grade without any purification.

2.2. Synthesis of K-OMS-2 and Ce/KM nanorods

The K^+ modified cryptomelane-type octahedral molecular sieve (K-OMS-2) nanorods support was synthesized by a feasible hydrothermal treatment. Firstly, $KMnO_4$ (1.66 g) and $MnSO_4{\cdot}H_2O$ (2.48 g) were mixed in deionized water (75 mL). Then the suspension was added into a Teflon-lined autoclave (150 mL), which was sealed and kept in an oven at 160 ℃ for 4 h. After the autoclave was cooled to the room temperature, the black slurry was filtered, washed with deionized water and ethanol for five times, and dried at 110 ℃ overnight. Finally, the final photocatalyst was calcinated in air at 300 ℃ for 6 h.

CeO_2 nanoparticles was obtained by calcinating $Ce(NO_3)_3{\cdot}6H_2O$ in air at 350 ℃ for 3 h. Ce/KM nanorods were fabricated by wet impregnation method. Typically, a required amount of $Ce(NO_3)_3{\cdot}6H_2O$ was dissolved in the mixture of H_2O and HAc (V_{H2O}:V_{HAc} = 20:1). Subsequently, K-OMS-2 nanorods was added into the solution and the molar ratio $n_{(Ce)}/n_{(Mn)}$ of 10 % was selected through activity filtering and literature [11,52]. The above suspension was kept in an oil bath under stirring until dryness, and further fully dried in an oven at 110 ℃ overnight, followed by thermal treatment in air at 350 ℃ for 3 h.

2.3. Synthesis of 0-OMS-2 and Ce/0M nanorods

In order to compare and explore the effect of K^+, 0-OMS-2 samples without K^+ and composites were prepared. However, the 0-OMS-2 via the ion exchange method of K-OMS-2 cannot be successfully synthesized and it was unable to obtain very pure potassium-free samples. According to the literature [34,53], the cryptomelane-type octahedral molecular sieve (0-OMS-2) nanorods support without K^+ modified and was synthesized by a feasible hydrothermal treatment.

Firstly, $MnSO_4{\cdot}H_2O$ (1.35 g), $(NH_4)_2S_2O_8$ (1.83 g) and $(NH_4)_2SO_4$ (1.98 g) were mixed in deionized water (40 mL). Then the suspension was added into a Teflon-lined autoclave (100 mL), which was sealed and kept in an oven at 120 ℃ for 20 h. After the autoclave was cooled to the room temperature, the black slurry was filtered, washed with deionized water and ethanol for five times, and dried at 110 ℃ overnight. Finally, for consistency, the roasting temperature was the same as K-OMS-2, the final photocatalyst was calcinated in air at 300 ℃ for 4 h to eliminate the influence.

CeO_2 nanoparticles was obtained by calcinating $Ce(NO_3)_3{\cdot}6H_2O$ in air at 350 ℃ for 3 h. Ce/0M nanorods were fabricated by wet impregnation method. Typically, a required amount of $Ce(NO_3)_3{\cdot}6H_2O$ was dissolved in the mixture of H_2O and HAc (V_{H2O}:V_{HAc} = 20:1). Subsequently, 0-OMS-2 nanorods was added into the solution, and the above

suspension was kept in an oil bath under stirring until dryness, and further fully dried in an oven at 110 ℃ overnight, followed by thermal treatment in air at 350 ℃ for 3 h. According to this method, 10 % molar ratios of CeO_2 to 0-OMS-2 nanorods were obtained and defined as Ce/0M.

2.4. Experimental setup

The X-ray diffraction (XRD) patterns of photocatalysts were collected on a Philips X'Pert Pro diffractometer using Ni-filtered Cu-Kα radiation (λ = 1.5418 nm) with a tube current of 40 mA and a tube voltage of 40 kV. The surface morphology and microstructure of the photocatalysts were characterized on scanning electron microscope (SEM, SSX-550) under 30 kV. The particle size and lattice fringes were obtained on a transmission electron microscopy (TEM, Talos F200X and JEM-2100) under 200 kV. The surface chemical compositions and VB as well as electric states were examined by X-ray photoelectron spectroscopy (XPS) with a PHI 5000 Versa Probe high performance electron spectrometer, an Al Kα radiation achromatic X-ray source at 1486.6 eV. The carbonaceous C 1 s line at 284.6 eV as the reference to calibrate total binding energies has ± 0.1 eV experimental errors. The optical absorption properties were recorded using a UV–vis spectrophotometer diffuse reflectance spectroscopy (DRS, UV-2401, Shimadzu) with the reference of $BaSO_4$, ranging from 200 nm to 800 nm. Photoluminescence (PL) spectra were carried out using a FluroMax-4 fluorescence spectrophotometer with the wavelength of the excitation light of 325 nm at room temperature in the solid state. The *in situ* electron spin resonance (ESR) measurements were taken on a JES FA200 spectrometer with 5,5-dimethyl-1-pyrroline-*N*-oxide (DMPO, 100 mM) as solvent, and the *in situ* ESR spectra of Ce/KM at N_2 or O_2 atmosphere were carried out at 77 K to determine the signal of Ce^{3+} species. O_2-temperature-programed desorption (O_2-TPD) experiments was carried out in a fixed-bed quartz flow reactor connected with a mass spectrograph (MS). Raman spectra were carried out on a LabRAM Aramis (Japan Horiba) Laser Raman spectrometer under an excitation source of Ar^+ lasers at 532 nm. *In situ* diffuse reflectance infrared Fourier transform (*in situ* DRIFT) spectra were collected on a Nicolet Nexus 5700 FTIR spectrometer by an MCT detector, and the resolution of spectra was 4 cm^{-1}. The *in situ* DRIFT spectra were obtained under 300 W Xenon lamp irradiation and toluene (balanced by high-purity air) gas. The catalyst after photocatalytic toluene oxidation was added to 2 mL ethyl acetate and ultrasonicated for 30 min. The suspension was filtered, and the filtrate was further tested by gas chromatography-mass spectrometer (GC–MS, ISQ, Thermo) and the pure He was used as mobile phase.

The photoelectrochemical measurements were conducted on a CHI660E electrochemical workstation equipped with a standard three-electrode cell. The photocatalytic sample was applied on fluorine-doped Tin Oxide (FTO) function as the working electrode and platinum wire electrode and Ag/AgCl electrode were considered as the counter and reference electrodes, respectively, and the test condition was contrasted according to references [54,55]. Meanwhile, the electrolyte solution was Na_2SO_4 (0.1 M) and the light source was a Xenon arc lamp. In the on–off cycles of illumination, the transient photocurrent response was collected at 0.5 V versus Ag/AgCl.

2.5. Photocatalytic toluene oxidation

The photocatalytic oxidation of toluene was carried out in a 1.5 L cylindrical reactor, using a light source of a 300 W Xenon lamp. Typically, the catalyst powder (50 mg) was uniformly dispersed on 304 stainless steel mesh. The toluene (85 mL·min^{-1}) was brought out by high-purity air (21 % O_2, N_2 balanced) into the reactor with specific relative humidity. After adsorption in dark for 40 min, the photocatalytic toluene oxidation under the 300 W Xenon lamp irradiation were determined.

2.6. DFT calculation

The Vienna Ab Initio Package (VASP) was employed to perform all the density functional theory (DFT) calculations within the generalized gradient approximation (GGA) using the Perdew-Burke Emzerhof (PBE) formulation [56–58]. The projected augmented wave (PAW) potentials were chosen to describe the ionic cores [59,60]. Taking valence electrons into account, a plane wave basis was used set with a kinetic energy cutoff of 400 eV. Partial occupancies of the Kohn-Sham orbitals were allowed using the Gaussian smearing method and a width of 0.05 eV. The electronic energy was considered self-consistent when the energy change was smaller than 10^{-5} eV. A geometry optimization was considered convergent when the force change was smaller than 0.02 eV/Å. Grimme's DFT-D3 methodology was used to describe the dispersion interactions [61]. The on-site corrections (DFT + U) has been applied to the 3d electrons of Mn atoms (U_{eff} = 5.2 eV) and 4f electrons of Ce atoms (U_{eff} = 4.5 eV) by the approach from Dudarev *et al.* [62].

The equilibrium lattice constants of tetragonal α-MnO_2 unit cell were optimized, when using a 3 × 3 × 11 Monkhorst-Pack k-point grid for Brillouin zone sampling, to be a = b = 9.695 Å, c = 2.905 Å. The equilibrium lattice constant of cubic CeO_2 unit cell was optimized, when using a 11 × 11 × 11 Monkhorst-Pack k-point grid for Brillouin zone sampling, to be a = 5.479 Å. We then use it to construct an α-MnO_2(3 1 0)/CeO_2(1 1 1) heterojunction model. For the α-MnO_2(3 1 0) part, it has the p(1 × 7) periodicity in the x and y directions and 2 stoichiometric layers in the z direction; for the CeO_2(1 1 1) part, it has the p(8 × 3 $\sqrt{3}$) periodicity in the x and y directions and 2 stoichiometric layers in the z direction. And the heterojunction slab was separated by a vacuum layer in the depth of 15 Å in order to separate the surface slab from its periodic duplicates. The mismatch at the × direction and y direction is as small as 3.8 % and 1.0 %, respectively. This model contains 112 Mn, 96 Ce and 416 O atoms, which are corresponding to the results of inductive coupled plasma emission (ICP) Spectrometer in Table S1. During structural optimizations, the gamma point in the Brillouin zone was used for k-point sampling, and all atoms were allowed to relax.

3. Results and discussion

3.1. Morphological, structural and compositional information

The morphology and nanostructures were examined by TEM in Fig. 1a, f and SEM in Fig. S1 (Supporting data), respectively, which showed that the K-OMS-2 and Ce/KM photocatalysts exhibited regular nanosized rods, and the diameter of as-synthesized K-OMS-2 nanorods measured about 25 nm while the length was irregular. The elemental energy-dispersive system (EDS) mapping of Ce/KM nanorods shows the highly uniform distribution of Ce, K, Mn and O (Fig. 1b-e). The rough surface of Ce/KM nanorods revealed that CeO_2 nanoparticles were successfully loaded. The HRTEM were used to determine the nanostructures and lattice fringes of the as-synthesized Ce/KM photocatalysts (Fig. 1f), which suggested that CeO_2 nanoparticles were growing on the surface of Ce/KM.

The phase structures of as-synthesized pure 0-OMS-2, Ce/0M, K-OMS-2 and Ce/KM photocatalysts composites as well as pure CeO_2 were investigated by XRD characterization. As shown in Fig. S2, for 0-OMS-2 and K-OMS-2, the diffraction peaks at *ca.* 18.18°, 12.74°, 28.70°, 37.72°, 42.12° and 60.06° are indexed as the (2 0 0), (2 2 2), (3 1 0), (2 1 1), (3 0 1), (5 2 1) crystal planes of OMS-2 (JCPDS no: 29-1020), respectively. While, for CeO_2 nanoparticles, the intensity of the diffraction peaks at *ca.* 28.58°, 47.40°, 56.26°, 33.08°, 76.68° and 69.32° are indexed as the (1 1 1), (2 2 0), (3 1 1), (2 0 0), (3 3 1), (4 0 0) crystal planes of the CeO_2 (JCPDS no: 34-0394), respectively. It was found that for the composite samples, the diffraction peaks of CeO_2 were not obvious, but in TEM and HRTEM images, the CeO_2 particles and its exposed crystal faces could be observed. Generally, small particles are not detected by

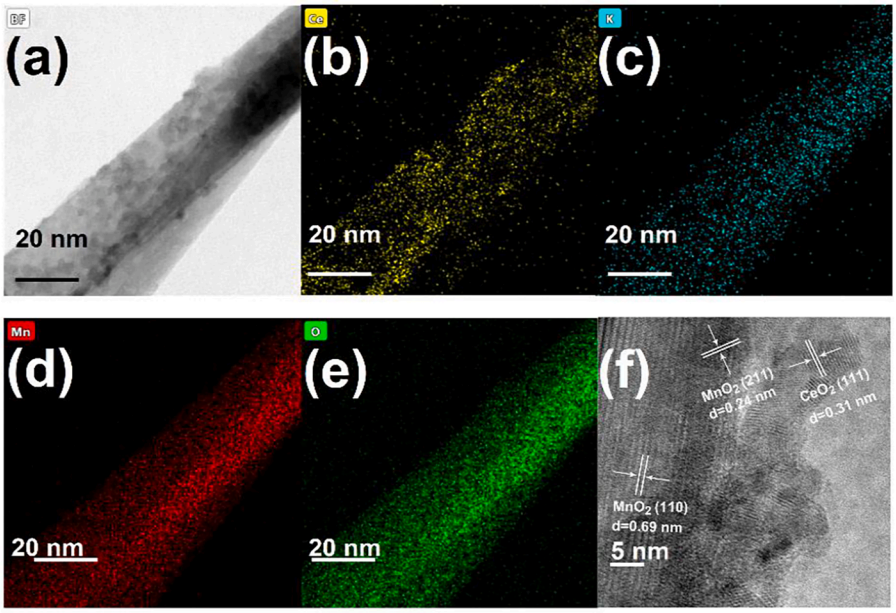

Fig. 1. The TEM image (a) of Ce/KM and the corresponding elemental mapping images of Ce, K, Mn and O of Ce/KM (b-e); The HRTEM image (f) of Ce/KM.

the XRD method, because of the determine limitation. Furthermore, the X-ray Fluorescence (XRF) Spectrometry result of Ce/0M and Ce/KM was showed in Table S2 to directly prove the loading of CeO_2. Therefore, combining with the results of HRTEM and XRD characterizations, it was justified to declare the successful loading of CeO_2 on OMS-2.

3.2. Photocatalytic performance of toluene

The photocatalytic toluene oxidation was carried out under full spectrum radiation, as shown in Fig. 2. The presence of water vapor helped to generate more reactive species such as hydroxyl radicals during the photocatalytic reaction. Excessive water content easily covered the catalyst surface active sites and affected the adsorption of toluene. Therefore, relative humidity (RH) was first roughly tested to determine the water content that was most favorable for the catalytic reaction. Obviously, the catalyst showed the best catalytic activity when the RH was around 18 %, and further research was carried out based on this condition. It depicted clearly in Fig. 2b that the toluene conversion was ordered by Ce/KM > K-OMS-2 > Ce/0M > 0-OMS-2, and the samples with K^+ exhibited better conversion of toluene and stability than 0-OMS-2 and Ce/0M, which illustrated the important role of K^+ in photocatalytic performance. From the other aspect, with the degradation process, the toluene conversion of K-OMS-2 decreased from 80.73 to 60.86 %, which suggested that it provided with poorer stability, while Ce/KM remained almost unchanged activity. Furthermore, the product of CO_2 concentrations in Fig. 2c also show that Ce/KM nanorods was provided with the best photocatalytic performance of toluene oxidation. To prove the stability, three cycle tests of photocatalytic toluene oxidation of Ce/KM were performed in Fig. S3. After three catalytic cycles, Ce/KM showed the excellent stability of toluene oxidation. In addition, the photocatalytic activities of related MnO_2 and CeO_2-based photocatalysts in literatures were list in Table S3. It could be found that the photocatalytic performance of Ce/KM was more excellent or comparable with the reported MnO_2 and CeO_2-based photocatalysts for toluene oxidation. Generally, the photocatalytic activity was closely related to the heterojunction structure, leading to the available directional transfer of photogenerated charges. While, the stability was resulted from the surface adsorption active oxygen species, oxidized free radicals, etc. Therefore, the improved photocatalytic activity and stability with the help of K^+ and CeO_2 were investigated and discussed, respectively.

3.3. Key roles of K^+

The formation of heterojunction types was closely related to the Fermi levels of two individuals in the composition. Therefore, the Fermi levels of 0-OMS-2 (without K^+), K-OMS-2 and CeO_2 were analyzed by DFT calculations, in order to explore the heterojunction structures and roles of K^+ in Ce/KM and Ce/0M. The specific difference of the Fermi levels of 0-OMS-2, K-OMS-2 and CeO_2 had been shown in Fig. S4 in the form of a schematic diagram. For Ce/0M, the Fermi level of 0-OMS-2 in Fig. 3a was higher than CeO_2, and then for Ce/0M, the photo-generated

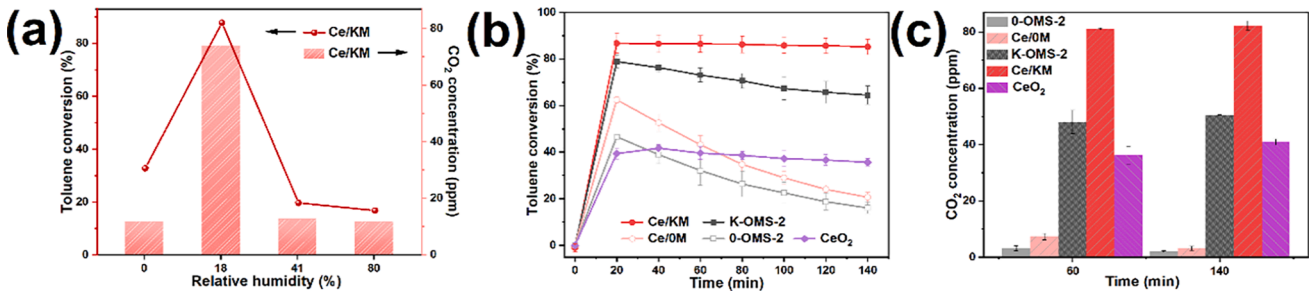

Fig. 2. The photocatalytic performances of Ce/KM under different relative humidity (a); Photocatalytic activities (b) and CO_2 concentrations (c) of 0-OMS, Ce/0M, K-OMS-2, Ce/KM and CeO_2.

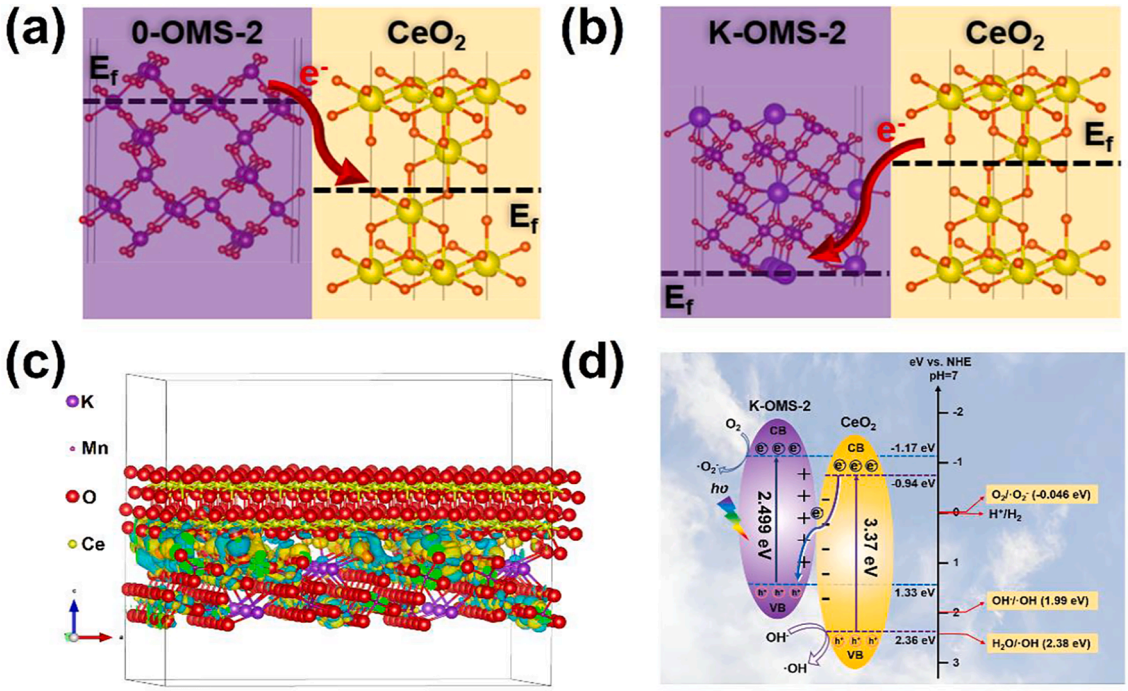

Fig. 3. Schematic diagrams of relative Fermi levels of Ce/KM (a) and Ce/0M (b), respectively. (c) DFT calculation of Ce/KM. (d) Schematic diagram of the mechanism of free radical generation and band structure of Ce/KM.

electrons of 0-OMS-2 are facilitated to transfer to CeO_2 in light. Whereas, for Ce/KM, the Fermi level of K-OMS-2 was lower than CeO_2, which meant the opposite direction in Fig. 3b, *i.e.*, the photo-generated electrons are facilitated to transfer from CeO_2 to K-OMS-2 in light. The VB-XPS and M-S results of K-OMS-2 and CeO_2 were depicted in Fig. S5a-d, respectively. The VB values of K-OMS-2 and CeO_2 are 1.33 and 2.36 eV, respectively. The calculated results from the M-S plots of the flat band potentials for K-OMS-2 and CeO_2 were reckoned up to be −1.60 and −1.17 V (vs Ag/AgCl), which were −0.97 and −0.54 V (vs NHE), respectively. Usually, the flat band potentials of *n*-type semiconductors were 0.1–0.3 eV more positive than the CB potentials [63]. Consequently, the E_{CB} of K-OMS-2 in this paper was about −1.17 V (vs NHE). Whereas for CeO_2, the CB laid at −0.74 eV (vs NHE). These values of VB and CB were consistent with previous literature [36,41,45]. Combined with the calculation results of Fermi levels, it could be proposed that owing to the presence of K^+, Z-scheme heterojunction formed on Ce/KM, whereas type II heterojunction was on Ce/0M without K^+.

Furthermore, the difference in charge densities on the Ce/KM interface confirmed the formation of Z-scheme heterojunction by describing the interfacial electronic interactions without light. In Fig. 3c, yellow colors represent the increased electrons while the cyan colors are converse. It could be observed that on the interface of Ce/KM, the electrons were decreased in K-OMS-2 and increased in CeO_2, which suggested that the interfacial built-in electric field formed on Ce/KM, that was, the interfacial electrons from CeO_2 to K-OMS-2 without light. The photo-generated electrons flowed into K-OMS-2 under interfacial electrostatic attraction in light irradiation and the possible schematic diagram of the mechanism of free radical generation and band structure of Ce/KM was displayed in Fig. 3d. Therefore, Z-scheme heterojunction formed on Ce/KM with K^+ as charge modulation part in the built-in electronic field, and played as an available directional transfer of photogenerated charges.

Transient photocurrent responses, PL spectra and EIS Nyquist plots were carried out to confirm the formed built-in electronic field on Ce/KM with charge modulation of K^+ improved the separation and transfer of photogenerated charges. The transient photocurrent responses were conducted and ran five on–off cycles with a Xenon arc lamp illumination (Fig. S6a). It was clearly depicted that Ce/KM performed salient photocurrent response intensity, much better than Ce/0M. The improvement in the photogenerated electron-hole generation rate of K-OMS-2 and Ce/KM could contribute to the charge modulation part of K^+ in the built-in electronic field. As shown in Fig. S6b, PL spectra of Ce/KM composite displayed weaker PL emission peaks than that of Ce/0M, proving Ce/KM was better in the suppressing the photogenerated electron-hole pair recombination and displayed excellent performance in charge separation efficiency. In addition, the EIS Nyquist plots were compared. Generally, the smaller arc radius is corresponding to smaller charge transfer resistance. Ce/KM displayed smallest arc radius and performed the lowest charge transfer resistance, indicating that the combination of K-OMS-2 and CeO_2 can greatly accelerate electron transfer.

On the basis of the above characterizations, because of the presence of K^+, Ce/KM was provided with the built-in electronic field and Z-scheme heterojunction. K^+ as a charge modulation part kinetically promoted the photo-generated charge migration, which was beneficial for the enhanced photocatalytic toluene oxidation.

3.4. Adsorption and activation ability of O_2

Generally, for the ring opening process of toluene oxidation and the photocatalyst stability, the active free radicals are of great importance. Because Ce/KM had better stability than that of K-OMS-2 nanorods, the *in situ* electron spin resonance (*in situ* ESR) spectra were collected to determine hydroxyl radicals (•OH) and superoxide radical ($\bullet O_2^-$) under light irradiation. In Fig. 4a, it was revealed that with 10 min illumination of Xenon lamp, a number of •OH radicals were generated on Ce/KM, whereas few radicals were observed on K-OMS-2. The above phenomenon also showed in the results of $\bullet O_2^-$ (Fig. 4b). The different abilities of free radical generation explained the superior activity of Ce/KM, which was resulted from Z-scheme heterojunction with advantageous VB and CB positions, and thermodynamically increased richer free radical to mineralize toluene.

The better photocatalytic stability of Ce/KM than that of K-OMS-2 was closely related to the oxidation species in reaction, and the adsorbed

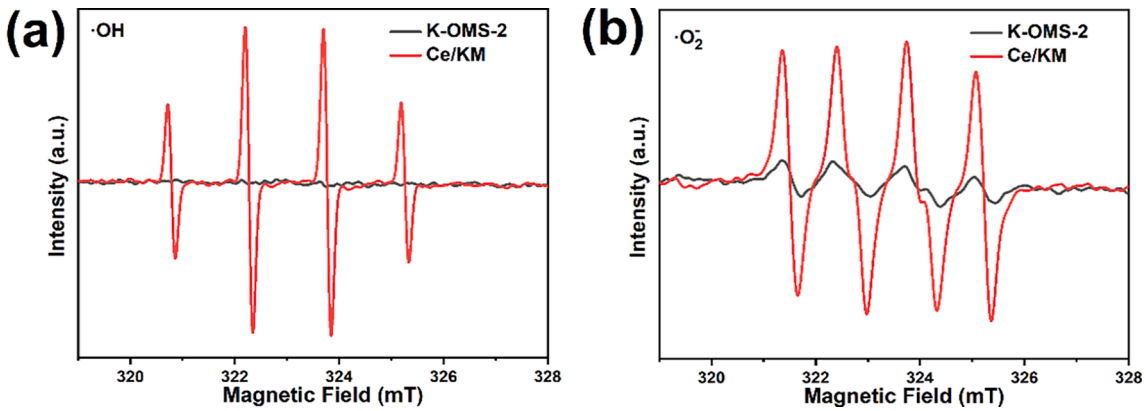

Fig. 4. *In situ* ESR spectra of K-OMS-2 and Ce/KM in aqueous dispersion for DMPO-•OH (a) and in methanol dispersion for DMPO-•O_2^- (b) under light irradiation.

active oxygen species and oxygen migration ability were important [26,64,65]. Therefore, Raman, O_2-TPD, and XPS experiments were detected. The Raman spectra of K-OMS-2 and Ce/KM were collected (Fig. 5a). On the Ce/KM composites, a broader band approximately centered at *ca.* 1050 cm^{-1} assigned to the O—O bond stretching in super-oxygen species on surface was observed [66–68]. Whereas, the signal was not found on K-OMS-2, which further confirmed that more adsorbed active oxygen species on Ce/KM surface, leading to active oxygen species participating in toluene oxidation.

Furthermore, the generation of active free radicals are related to the ability of oxygen migration, and O_2-TPD profiles of K-OMS-2 and Ce/KM composites were collected. As shown in Fig. 5b, the O_2 desorption peaks ranging from 250 to 650 ℃. According to the previous literature, the broad peak was composed of the desorption peaks of surface oxygen (O_{surf}) species and lattice oxygens (O_{latt}) species [69–72]. The O_{surf} peak centered at 523.3 ℃ for K-OMS-2, while 491.8 ℃ for Ce/KM, respectively. It could be found that the onset O_2 desorption temperature of Ce/KM at around 328.3 ℃ was lower than that of pure K-OMS-2 at *ca.* 346.2 ℃, and the peak area ratio of O_{surf} of Ce/KM (61.6 %) was higher than that of K-OMS-2 (46.2 %), illustrating that richer surface adsorbed oxygen species with better mobility were achieved on Ce/KM, thus leading to richer active free radicals. Furthermore, the results of XPS O1s of samples were shown in Fig. S7 to investigate the surface oxygen species and the peak area ratios were shown in Table S4. It was revealed the surface oxygen and oxygen vacancies of Ce/KM were higher than that of K-OMS-2, suggesting that the loading of CeO_2 was facilitated to forming more oxygen defects and surface oxygen species, consistent with the results of O_2-TPD.

Combining the results of active free radicals with the properties of storage-release oxygen and redox of CeO_2, it was proposed that CeO_2 played an important role on the adsorption and activation capacity of oxygen. Therefore, the *in situ* ESR under different atmospheres were carried out on Ce/KM, respectively, to confirm the adsorption site of oxygen. In Fig. 5c, the signal of g = 1.93 corresponded to Ce^{3+}, and the signal of g ≈ 1.96 originated from □-Ce^{3+}-O-Ce^{4+} [67,73,74]. The Ce^{3+} species remained unchanged under the illumination of N_2, whereas when the atmosphere was high-purity oxygen, the signals of the Ce^{3+} species and the □-Ce^{3+}-O-Ce^{4+} decreased, indicating that O_2 was adsorbed on Ce^{3+} of CeO_2.

Moreover, the fresh catalysts (the synthesized samples) and used catalysts testing by photocatalytic toluene oxidation for 140 min were compared to show the photocatalytic stability. The chemical state of surface Mn atoms was explored by XPS and results were listed in Table S5. In the fresh K-OMS-2 and Ce/KM, the ratios of Mn^{4+}/Mn^{3+} were similar, *i.e.*, 13.77 % and 13.69 %, respectively. However, after photocatalytic degradation of toluene, the used Ce/KM had the Mn^{4+}/Mn^{3+} ratio increasing from 13.69 to 14.63 %, while that of the used K-OMS-2 increased from 13.77 to 17.03 %. Generally, more Mn^{4+} species suggested fewer oxygen vacancies. More Mn^{4+} species on the used K-OMS-2 indicated the more consumption of oxygen vacancies in reaction, which might be attributed to strong adsorption of intermediates and catalyst poisoning. However, due to the interleaved *4f-5d* orbitals of Ce in favor of the supplement of Mn^{3+}, Ce/KM exhibited better stability.

Combining the above-mentioned results, it was deduced that the toluene deep-oxidation activity and stability of K-OMS-2 could be significantly promoted by CeO_2 modification owing to the easy valence switching of $Ce^{3+/4+}$, the formation of surface adsorbed oxygen species, improved oxygen mobility, enhanced oxygen adsorption and more active free radicals.

3.5. Proposed mechanism of photocatalytic toluene oxidation

In situ DRIFTS is considered to be a powerful characterization to explore the reaction mechanism. And it is necessary to further confirm the reason why the modification of CeO_2 was beneficial to promote the photocatalytic stability of Ce/KM. Therefore, to track and verify the evolution of reactants, *in situ* DRIFTS of toluene adsorption were carried out. As shown in Fig. 6a and b, adsorption bands at 1461 cm^{-1} attributed

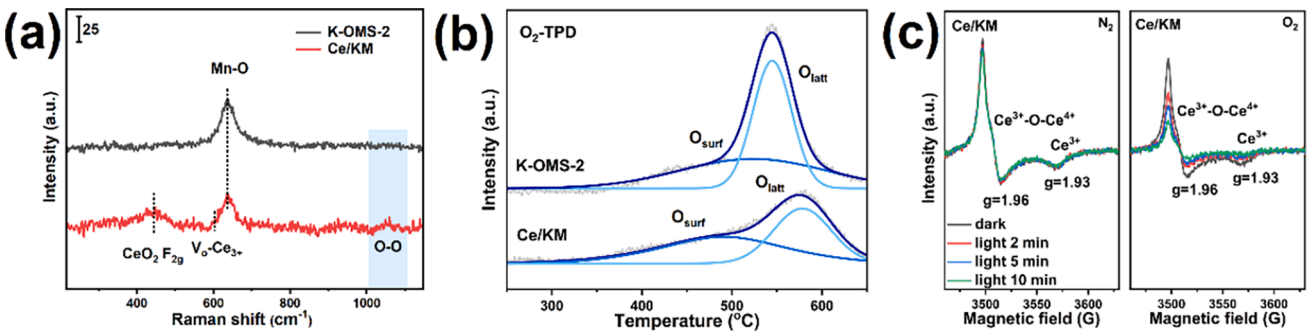

Fig. 5. Raman spectra (a) and O_2-TPD profiles (b) of K-OMS-2 and Ce/KM; *in situ* ESR spectra of Ce/KM at N_2 or O_2 atmosphere.

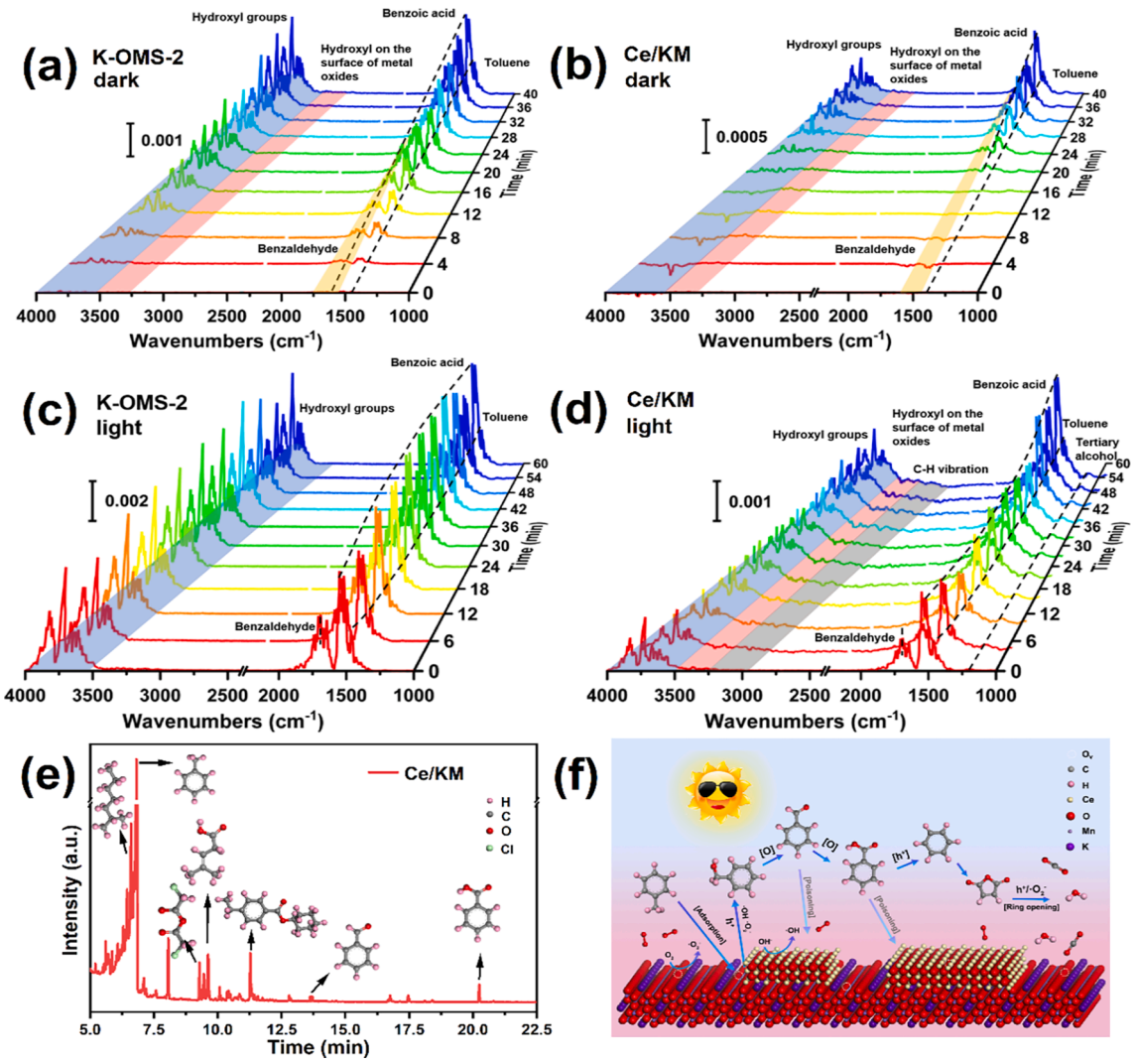

Fig. 6. *In situ* DRIFTS of toluene oxidation over K-OMS-2 (a) and Ce/KM (b) in dark, and K-OMS-2 (c) and Ce/KM (d) in light irradiation; (c) The reaction intermediate products detected by GC–MS during the toluene oxidation process over Ce/KM; (d) Schematic illustration of proposed mechanisms for toluene oxidation over the Ce/KM catalyst.

to adsorbed toluene were observed on both samples in dark [75–77]. The bands at 1540 and 3600 ~ 4000 cm^{-1} were attributed to benzoic acid and hydroxyl groups on the catalysts [77,78]. Comparing to Ce/KM, the bands on K-OMS-2 were more intensive, suggesting that K-OMS-2 could better facilitate the adsorption of toluene and H_2O, which might be due to the higher electron mobility of K-OMS-2 and easier strong adsorption of toluene molecules and water [76–78]. Based on the result, it was proposed that the toluene was adsorbed on K-OMS-2. Furthermore, the role of K^+ in toluene adsorption and activation were discussed, and the comparison of toluene adsorption on 0-OMS-2 and K-OMS-2 were in Fig. S8. The peaks at 1429, 1469 and 1513 cm^{-1} were attributed to adsorbed toluene, according to the rulers of spectra, it was observed that the K-OMS-2 displayed more toluene adsorption than that of 0-OMS-2 [76]. Furthermore, the strong peak at 1540 cm^{-1} was attributed to carboxyl signal of benzoic acid, which was on K-OMS-2, not on 0-OMS-2 [64]. And the hydroxyl group bands above 3600 cm^{-1}, were more intensive on K-OMS-2 than that on 0-OMS-2. According to literature, hydroxyl groups on catalysts could adsorb toluene via strong OH-π bonds, which is further activated and oxidized into benzoic acid [7–9]. Due to the charge balance, the electronic effect of K^+ increased the proportion of Mn^{3+}, which promoted the generation of hydroxyl groups and thus the adsorption and activation of toluene were enhanced [78,79].

Moreover, *in situ* DRIFTS of toluene adsorption in light were carried out. Once the Xenon lamp turned on, the peaks at 1461 and 1517 cm^{-1} of toluene and 1542 and 1560 cm^{-1} of benzoic acid were intensive, especially K-OMS-2 in Fig. 6c and c [64,75,76,78,80,81]. However, excessive strong adsorption of reaction intermediates could easily cover the reactive sites and was not conducive to the progress of the reaction. Besides, it was noteworthy that the peak centered at 1200 cm^{-1} and 3100 ~ 3000 cm^{-1} was detected which originated from tertiary alcohol and -C═C–H, reveling the stronger capability of opening loop of Ce/KM [82,83]. The loading of CeO_2 helped produce more free radicals and active oxygen species on Ce/KM and improve stronger opening loop ability as well as deep oxidation of toluene [64].

Furthermore, the degradation pathway of photocatalytic toluene was investigated by GC–MS to identify gas phase products of Ce/KM. In Fig. 6e, the dominated the gas phase products and some incompletely oxidized intermediate products were found, including benzaldehyde, benzoate, branched alkanes and cyclohexanol p-ethyl benzoate. Combined with the results of *in situ* DRIFTS, the reaction pathways for photocatalytic toluene oxidation over Ce/KM could be proposed (Fig. 6f). Firstly, toluene molecules were adsorbed and activated on the K-OMS-2 surface of Ce/KM interface, due to the d orbit electrons of Mn^{3+} donating to methyl of toluene [64]. Subsequently, under light irradiation, owing to the K^+ and Z-scheme heterojunction, the photo-

generated holes and electrons were generated on CeO_2 and K-OMS-2 in the interface, respectively, which interacted with adsorbed oxygen species to generated •OH and $\bullet O_2^-$, and then attacked adsorbed toluene molecules in the interface. Methyl and benzene ring of toluene were oxidized to maleic anhydride, which opened the ring to small molecular substances, and finally mineralized into carbon dioxide and water.

In addition, the appropriate relative humidity was significant to photocatalytic toluene oxidation and the effect of H_2O was needed to be investigated and the *in situ* DRIFTS and GC–MS characterizations were employed. In Fig. 7, *in situ* DRIFTS of toluene adsorption in dark and light irradiation over Ce/KM under the reaction condition without/with H_2O were determined, respectively. Comparing the absorption on the Ce/KM without H_2O (Fig. 7a) and without H_2O (Fig. 7b) under dark, it was evident that under the same ruler of spectra, there were more hydroxyl groups at 3740 cm^{-1} from H_2O, and hydroxyl on the surface at 3698 cm^{-1} and 3378 cm^{-1}, suggesting that the introduce of H_2O was beneficial for the generation of hydroxyl on the photocatalyst surface [20,77,78]. Besides, the peaks centered at 1452 cm^{-1} originated from toluene adsorption, and the bands at 3498, 1645 and 1567 cm^{-1} were attributed to benzyl alcohol, benzaldehyde and benzoic acid, respectively [76,84]. It was found that no signals about alcohols and more toluene adsorption were detected on Ce/KM without H_2O, and the appearance of benzaldehyde and benzoic acid was later than that with H_2O. The phenomenon suggested that with the help of H_2O, the adsorbed toluene can be quickly oxidized to benzaldehyde, benzyl alcohol, etc. in the case of dark, which showed stronger oxidizing ability than that without H_2O.

Once the light irradiation was introduced, on Ce/KM without H_2O (Fig. 7c), the peaks originated from toluene at 1452, 1517 cm^{-1} and benzoic acid at 1564, 1560 cm^{-1} were accumulated rapidly, suggesting that the formed active radical from photo-generated charges promoted the oxidation of toluene. While, as for the Ce/KM with H_2O (Fig. 7d), the hydroxyl on the surface of metal oxides at 3698 cm^{-1} were decreased, and the vibration peaks of C—H at 2700–3200 cm^{-1} from aldehyde groups and unsaturated carbon chains were increased in light irradiation, which showed that H_2O resulted in hydroxyls was facilitated to opening rings and deep oxidation, so that the toluene and intermediates absorbed on the surface of catalysts could be transferred quickly [20,80]. Therefore, from the results of *in situ* DRIFTS of toluene adsorption in dark and light irradiation under the reaction condition without/with H_2O, it was proposed that the introduce of H_2O was helpful for the generation of hydroxyls on photocatalyst surface, leading to the adsorption and activation of toluene via OH-π interactions and deep oxidation of toluene molecules. Due to the limitation of our *in situ* DRIFTS instrument, the relative humidity cann't be controlled, and the GC–MS spectra were used to investigate the effects of the relative humidity on the products in the reaction process.

The GC–MS method determined the products of photocatalytic toluene oxidation under the humidity of 0, 18 %, and 30 %, and the corresponding spectra were displayed in Fig. S9. Table S6 showed the intermediates identification of toluene photocatalytic oxidation by GC–MS. Combined the results of the relative peak intensities of three relative humidity, it could be found that under the relative humidity of 18 %, the relative contents of benzaldehyde and benzyl alcohol were significantly richer. In addition, a little ethyl benzoate under the humidity of 18 % were indicated that there was benzoic acid, which were not detected on the other humidity of 0 and 30 %. According to the literatures, the presence of water vapor helped to generate more oxidizing free radicals during the photocatalytic reaction, while excessive water easily covered the catalyst surface and affected the adsorption and activation of toluene [76,85]. Therefore, the appropriate humidity promoted the generation of hydroxyls and oxidizing free radicals on photocatalyst surface, leading to the adsorption and activation of toluene via OH-π interactions and deep oxidation of toluene molecules, while too higher humidity was not beneficial for the adsorption of toluene.

4. Conclusion

In summary, owing to the presence of K^+ and surface adsorbed

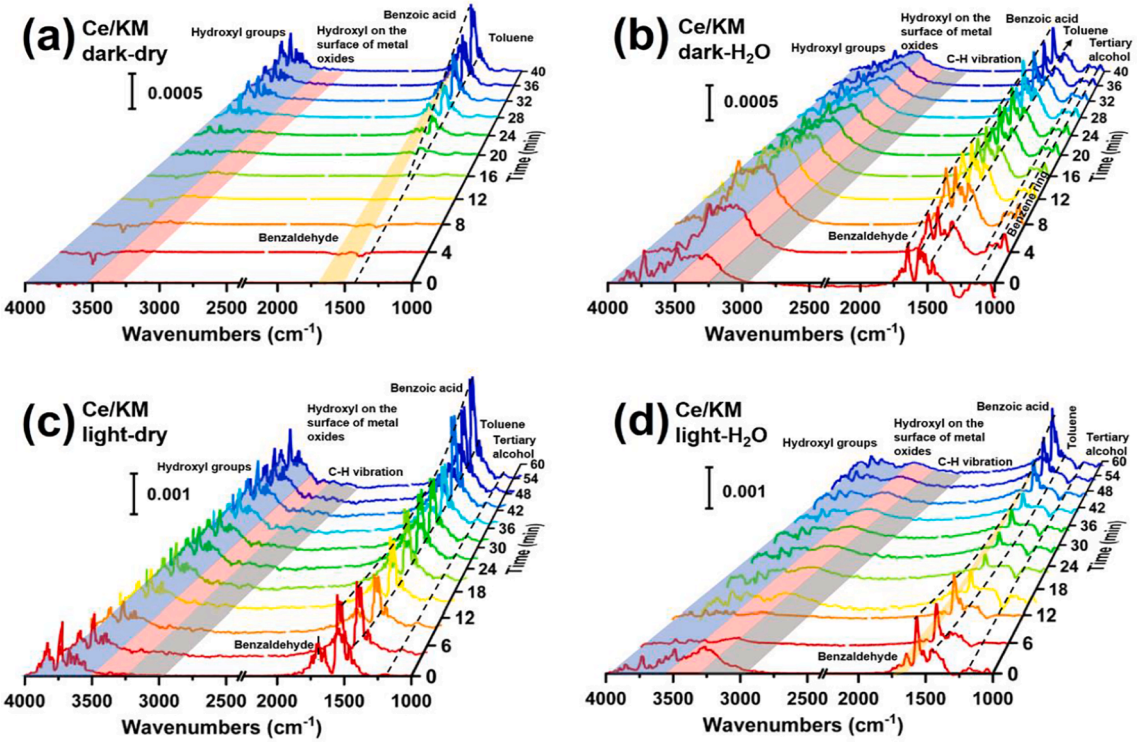

Fig. 7. *In situ* DRIFTS of toluene adsorption in dark and light irradiation over Ce/KM under the reaction condition without H_2O (a) (c) and with H_2O (b) (d), respectively.

oxygen species, Ce/KM photocatalyst was provided with more excellent activity and stability of photocatalytic toluene oxidation. For Ce/KM, K^+ had influences on Fermi level of OMS-2 and the increased proportion of Mn^{3+}, leading to the formation of Z-scheme heterojunction and hydroxyl groups, and achieved faster photo-generated charge transfer and intensive toluene adsorption. Furthermore, O_2 molecules adsorbed on Ce^{3+} and □-Ce^{3+}-O-Ce^{4+} of CeO_2, and Ce/KM exhibited richer active oxygen radicals and enhanced oxygen migration. In addition, the humidity is important, because appropriate humidity promoted the generation of hydroxyls and oxidizing free radicals for deep toluene oxidation.

Declaration of Competing Interest

The authors declare that they have no known competing financial interests or personal relationships that could have appeared to influence the work reported in this paper.

Data availability

Data will be made available on request.

Acknowledgements

W.Z. and L.D. would like to acknowledge the support of the National Natural Science Foundation of China (21972062) and Fundamental Research Funds for the Central Universities (21114380163).

Appendix A. Supplementary data

Supplementary data to this article can be found online at https://doi.org/10.1016/j.cej.2022.138943.

References

[1] J. Qu, D. Chen, N. Li, Q. Xu, H. Li, J. He, J. Lu, Ternary photocatalyst of atomic-scale Pt coupled with MoS2 co-loaded on TiO2 surface for highly efficient degradation of gaseous toluene, Appl. Catal. B 256 (2019), 117877.
[2] Z. Wang, P. Ma, K. Zheng, C. Wang, Y. Liu, H. Dai, C. Wang, H.-C. Hsi, J. Deng, Size effect, mutual inhibition and oxidation mechanism of the catalytic removal of a toluene and acetone mixture over TiO2 nanosheet-supported Pt nanocatalysts, Appl. Catal. B 274 (2020), 118963.
[3] A.H. Mamaghani, F. Haghighat, C.-S. Lee, Gas phase adsorption of volatile organic compounds onto titanium dioxide photocatalysts, Chem. Eng. J. 337 (2018) 60–73.
[4] Z. Wang, S. Xie, Y. Feng, P. Ma, K. Zheng, E. Duan, Y. Liu, H. Dai, J. Deng, Simulated solar light driven photothermal catalytic purification of toluene over iron oxide supported single atom Pt catalyst, Appl. Catal. B Environ. (2021), 120612.
[5] A.H. Mamaghani, F. Haghighat, C.-S. Lee, Photocatalytic oxidation technology for indoor environment air purification: The state-of-the-art, Appl. Catal. B 203 (2017) 247–269.
[6] F. Hu, Y. Peng, J. Chen, S. Liu, H. Song, J. Li, Low content of CoOx supported on nanocrystalline CeO2 for toluene combustion: The importance of interfaces between active sites and supports, Appl. Catal. B 240 (2019) 329–336.
[7] L. Wu, Z. Sun, Y. Zhen, S. Zhu, C. Yang, J. Lu, Y. Tian, D. Zhong, J. Ma, Oxygen vacancy-induced nonradical degradation of organics: critical trigger of oxygen (O2) in the Fe–Co LDH/peroxymonosulfate system, Environ. Sci. Technol. 55 (2021) 15400–15411.
[8] X. Zhang, X. Shi, Q. Zhao, Y. Li, J. Wang, Y. Yang, F. Bi, J. Xu, N. Liu, Defects controlled by acid-modulators and water molecules enabled UiO-67 for exceptional toluene uptakes: An experimental and theoretical study, Chem. Eng. J. 427 (2022), 131573.
[9] Y. Li, M. Wei, L. Liu, Q. Xue, B. Yu, Adsorption of toluene on various natural soils: Influences of soil properties, mechanisms, and model, Sci. Total Environ. 740 (2020), 140104.
[10] M. Malayeri, C.-S. Lee, J. Niu, J. Zhu, F. Haghighat, Kinetic modeling and reaction mechanism of toluene and by-products in photocatalytic oxidation reactor, Chem. Eng. J. 427 (2022), 131536.
[11] S. Mo, J. Li, R. Liao, P. Peng, J. Li, J. Wu, M. Fu, L. Liao, T. Shen, Q. Xie, D. Ye, Unraveling the decisive role of surface CeO2 nanoparticles in the Pt-CeO2/MnO2 hetero-catalysts for boosting toluene oxidation: Synergistic effect of surface decorated and intrinsic O-vacancies, Chem. Eng. J. 418 (2021), 129399.
[12] Z. Wang, H. Yang, R. Liu, S. Xie, Y. Liu, H. Dai, H. Huang, J. Deng, Probing toluene catalytic removal mechanism over supported Pt nano- and single-atom-catalyst, J. Hazard. Mater. 392 (2020), 122258.
[13] B. Yu, S. Zhang, X. Wang, Helical microporous nanorods assembled by polyoxometalate clusters for the photocatalytic oxidation of toluene, Angew. Chem. Int. Ed. 60 (2021) 17404–17409.
[14] M. Sleiman, P. Conchon, C. Ferronato, J.-M. Chovelon, Photocatalytic oxidation of toluene at indoor air levels (ppbv): Towards a better assessment of conversion, reaction intermediates and mineralization, Appl. Catal. B 86 (2009) 159–165.
[15] X. Wei, K. Li, X. Zhang, Q. Tong, J. Ji, Y. Cai, B. Gao, W. Zou, L. Dong, CeO2 nanosheets with anion-induced oxygen vacancies for promoting photocatalytic toluene mineralization: Toluene adsorption and reactive oxygen species, Appl. Catal. B 317 (2022), 121694.
[16] Z.-R. Tian, W. Tong, J.-Y. Wang, N.-G. Duan, V.V. Krishnan, S.L. Suib, Manganese oxide mesoporous structures: mixed-valent semiconducting catalysts, Science 276 (1997) 926.
[17] W. Yang, Y. Peng, Y. Wang, Y. Wang, H. Liu, Z. Su, W. Yang, J. Chen, W. Si, J. Li, Controllable redox-induced in-situ growth of MnO2 over Mn2O3 for toluene oxidation: Active heterostructure interfaces, Appl. Catal. B 278 (2020), 119279.
[18] P. Lu, L. Ye, X. Yan, P. Fang, X. Chen, D. Chen, C. Cen, Impact of toluene poisoning on MnCe/HZSM-5 SCR catalyst, Chem. Eng. J. 414 (2021), 128838.
[19] F.W. Boyom-Tatchemo, F. Devred, G. Ndiffo-Yemeli, S. Laminsi, E.M. Gaigneaux, Plasma-induced redox reactions synthesis of nanosized α-, γ- and δ-MnO2 catalysts for dye degradation, Appl. Catal. B 260 (2020), 118159.
[20] W. Yang, Z. Su, Z. Xu, W. Yang, Y. Peng, J. Li, Comparative study of α-, β-, γ- and δ-MnO2 on toluene oxidation: oxygen vacancies and reaction intermediates, Appl. Catal. B 260 (2020), 118150.
[21] P. Wu, X. Jin, Y. Qiu, D. Ye, Recent progress of thermocatalytic and photo/thermocatalytic oxidation for VOCs purification over manganese-based oxide catalysts, Environ. Sci. Technol. 55 (2021) 4268–4286.
[22] T. Chen, H. Dou, X. Li, X. Tang, J. Li, J. Hao, Tunnel structure effect of manganese oxides in complete oxidation of formaldehyde, Microporous Mesoporous Mater. 122 (2009) 270–274.
[23] X. Tang, J. Chen, X. Huang, Y. Xu, W. Shen, Pt/MnOx–CeO2 catalysts for the complete oxidation of formaldehyde at ambient temperature, Appl. Catal. B 81 (2008) 115–121.
[24] S.S.T. Bastos, J.J.M. Órfão, M.M.A. Freitas, M.F.R. Pereira, J.L. Figueiredo, Manganese oxide catalysts synthesized by exotemplating for the total oxidation of ethanol, Appl. Catal. B 93 (2009) 30–37.
[25] X. Tang, Y. Xu, W. Shen, Promoting effect of copper on the catalytic activity of MnOx–CeO2 mixed oxide for complete oxidation of benzene, Chem. Eng. J. 144 (2008) 175–180.
[26] C. He, J. Cheng, X. Zhang, M. Douthwaite, S. Pattisson, Z. Hao, Recent advances in the catalytic oxidation of volatile organic compounds: a review based on pollutant sorts and sources, Chem. Rev. 119 (2019) 4471–4568.
[27] Z. Sihaib, F. Puleo, J.M. Garcia-Vargas, L. Retailleau, C. Descorme, L.F. Liotta, J. L. Valverde, S. Gil, A. Giroir-Fendler, Manganese oxide-based catalysts for toluene oxidation, Appl. Catal. B 209 (2017) 689–700.
[28] L. Ye, P. Lu, X. Chen, P. Fang, Y. Peng, J. Li, H. Huang, The deactivation mechanism of toluene on MnOx-CeO2 SCR catalyst, Appl. Catal. B 277 (2020), 119257.
[29] R.J. Gritter, G.D. Dupre, T.J. Wallace, Oxidation of benzyl alcohols with manganese dioxide, Nature 202 (1964) 179–181.
[30] J. Hou, Y. Li, L. Liu, L. Ren, X. Zhao, Effect of giant oxygen vacancy defects on the catalytic oxidation of OMS-2 nanorods, J. Mater. Chem. A 1 (2013) 6736–6741.
[31] H. Deng, S. Kang, J. Ma, C. Zhang, H. He, Silver incorporated into cryptomelane-type Manganese oxide boosts the catalytic oxidation of benzene, Appl. Catal. B 239 (2018) 214–222.
[32] Q. Liu, Y. Xing, S. Xing, Y. Wu, B. Lu, S. Shi, Low-temperature o-xylene oxidation over KOH pre-modified OMS-2 catalyst: Dual effect of K on oxygen activation and carboxylate intermediate desorption, Appl. Surf. Sci. 569 (2021), 150974.
[33] N. Jiang, X. Li, X. Kong, Y. Zhao, J. Li, K. Shang, N. Lu, Y. Wu, The post plasma-catalytic decomposition of toluene over K-modified OMS-2 catalysts at ambient temperature: Effect of K+ loading amount and reaction mechanism, J. Colloid Interface Sci. 598 (2021) 519–529.
[34] J. Hou, L. Liu, Y. Li, M. Mao, H. Lv, X. Zhao, Tuning the K+ concentration in the tunnel of OMS-2 nanorods leads to a significant enhancement of the catalytic activity for benzene oxidation, Environ. Sci. Technol. 47 (2013) 13730–13736.
[35] P.Z.S. Zhifei Hao, Prof. Yi Li,Prof. Haitao Wang,Dr. Lirong Zheng,Ruihua Wang, Guoquan Liu,Prof. Sihui Zhan, The role of alkali metal in α-MnO2 catalyzed ammonia-selective catalysis, Angew. Chem., 58 (2019) 6351-6356.
[36] X. Li, G. Fang, X. Qian, Q. Tian, Z-scheme heterojunction of low conduction band potential MnO2 and biochar-based g-C3N4 for efficient formaldehyde degradation, Chem. Eng. J. 428 (2022), 131052.
[37] S. Zhou, Y. Wang, K. Zhou, D. Ba, Y. Ao, P. Wang, In-situ construction of Z-scheme g-C3N4/WO3 composite with enhanced visible-light responsive performance for nitenpyram degradation, Chin. Chem. Lett. 32 (2021) 2179–2182.
[38] P. Wang, J. Wang, J. Zhao, X. Ma, X. Du, S. Peng, X. Hao, B. Tang, A. Abudula, G. Guan, Trace holmium assisting delaminated OMS-2 catalysts for total toluene oxidation at low temperature, J. Colloid Interface Sci. 608 (2022) 1662–1675.
[39] P. Wu, S. Dai, G. Chen, S. Zhao, Z. Xu, M. Fu, P. Chen, Q. Chen, X. Jin, Y. Qiu, S. Yang, D. Ye, Interfacial effects in hierarchically porous α-MnO2/Mn3O4 heterostructures promote photocatalytic oxidation activity, Appl. Catal. B 268 (2020), 118418.
[40] E. Colman-Lerner, M.A. Peluso, J. Sambeth, H. Thomas, Cerium, manganese and cerium/manganese ceramic monolithic catalysts. Study of VOCs and PM removal, J. Rare Earths 34 (2016) 675–682.
[41] W. Li, L. Jin, F. Gao, H. Wan, Y. Pu, X. Wei, C. Chen, W. Zou, C. Zhu, L. Dong, Advantageous roles of phosphate decorated octahedral CeO2 {111}/g-C3N4 in

boosting photocatalytic CO2 reduction: Charge transfer bridge and Lewis basic site, Appl. Catal. B 294 (2021), 120257.
[42] G.-F. Zhou, J. Ma, S. Bai, L. Wang, Y. Guo, CO catalytic oxidation over Pd/CeO2 with different chemical states of Pd, Rare Met. 39 (2020) 800–805.
[43] J. Lv, Y. Shen, L. Peng, X. Guo, W. Ding, Exclusively selective oxidation of toluene to benzaldehyde on ceria nanocubes by molecular oxygen, Chem. Commun. 46 (2010) 5909–5911.
[44] N.S. Priya, C. Somayaji, S. Kanagaraj, Synthesis and characterization of Nd3+-doped Ce0.6Zr0.4O2 andits doping significance on oxygen storage capacity, Rare Met. 40 (2021) 231–236.
[45] X. Wei, X. Wang, Y. Pu, A. Liu, C. Chen, W. Zou, Y. Zheng, J. Huang, Y. Zhang, Y. Yang, M. Naushad, B. Gao, L. Dong, Facile ball-milling synthesis of CeO2/g-C3N4 Z-scheme heterojunction for synergistic adsorption and photodegradation of methylene blue: Characteristics, kinetics, models, and mechanisms, Chem. Eng. J. 420 (2021), 127719.
[46] J.M. López, A.L. Gilbank, T. García, B. Solsona, S. Agouram, L. Torrente-Murciano, The prevalence of surface oxygen vacancies over the mobility of bulk oxygen in nanostructured ceria for the total toluene oxidation, Appl. Catal. B 174–175 (2015) 403–412.
[47] Y. Liao, M. Fu, L. Chen, J. Wu, B. Huang, D. Ye, Catalytic oxidation of toluene over nanorod-structured Mn–Ce mixed oxides, Catal. Today 216 (2013) 220–228.
[48] D. Delimaris, T. Ioannides, VOC oxidation over MnOx–CeO2 catalysts prepared by a combustion method, Appl. Catal. B 84 (2008) 303–312.
[49] S. Putla, M.H. Amin, B.M. Reddy, A. Nafady, K.A. Al Farhan, S.K. Bhargava, MnOx nanoparticle-dispersed CeO2 nanocubes: a remarkable heteronanostructured system with unusual structural characteristics and superior catalytic performance, ACS Appl. Mater. Interfaces 7 (2015) 16525–16535.
[50] X. Wu, H. Yu, D. Weng, S. Liu, J. Fan, Synergistic effect between MnO and CeO2 in the physical mixture: Electronic interaction and NO oxidation activity, J. Rare Earths 31 (2013) 1141–1147.
[51] H. Liu, Y. Li, Y. Yang, Z. Shi, Q. Zhang, S. Wu, X. Zhao, Formation of CeMnxOy/OMS-2 nanocomposite significantly enhances UV–vis-infrared light-driven catalytic activity, Catal. Today 326 (2019) 46–53.
[52] L. Zhu, J. Wang, S. Rong, H. Wang, P. Zhang, Cerium modified birnessite-type MnO2 for gaseous formaldehyde oxidation at low temperature, Appl. Catal. B 211 (2017) 212–221.
[53] X. Wang, Y. Li, Selected-control hydrothermal synthesis of α- and β-MnO2 single crystal nanowires, J. Am. Chem. Soc. 124 (2002) 2880–2881.
[54] J. Zhang, B. Shen, Z. Hu, M. Zhen, S.-Q. Guo, F. Dong, Uncovering the synergy between Mn substitution and O vacancy in ZnAl-LDH photocatalyst for efficient toluene removal, Appl. Catal. B 296 (2021), 120376.
[55] Z. Zhao, B. Shen, Z. Hu, J. Zhang, C. He, Y. Yao, S.-Q. Guo, F. Dong, Recycling of spent alkaline Zn-Mn batteries directly: Combination with TiO2 to construct a novel Z-scheme photocatalytic system, J. Hazard. Mater. 400 (2020), 123236.
[56] G. Kresse, J. Furthmüller, Efficiency of ab-initio total energy calculations for metals and semiconductors using a plane-wave basis set, Comput. Mater. Sci. 6 (1996) 15–50.
[57] G. Kresse, J. Furthmuller, Efficient iterative schemes for ab initio total-energy calculations using a plane-wave basis set, Phys. Rev. B 54 (1996) 11169–11186.
[58] J.P. Perdew, K. Burke, M. Ernzerhof, Generalized gradient approximation made simple, Phys. Rev. Lett. 77 (1996) 3865–3868.
[59] G. Kresse, D. Joubert, From ultrasoft pseudopotentials to the projector augmented-wave method, Phys. Rev. B 59 (1999) 1758–1775.
[60] P.E. Blochl, Projector augmented-wave method, Phys. Rev. B 50 (1994) 17953–17979.
[61] S. Grimme, J. Antony, S. Ehrlich, H. Krieg, A consistent and accurate ab initio parametrization of density functional dispersion correction (DFT-D) for the 94 elements H-Pu, J. Chem. Phys. 132 (2010).
[62] S.L. Dudarev, G.A. Botton, S.Y. Savrasov, C.J. Humphreys, A.P. Sutton, Electron-energy-loss spectra and the structural stability of nickel oxide: An LSDA+U study, Phys. Rev. B 57 (1998) 1505–1509.
[63] N. Tian, H. Huang, C. Liu, F. Dong, T. Zhang, X. Du, S. Yu, Y. Zhang, In situ co-pyrolysis fabrication of CeO2/g-C3N4 n–n type heterojunction for synchronously promoting photo-induced oxidation and reduction properties, J. Mater. Chem. A 3 (2015) 17120–17129.
[64] Z. Su, W. Si, H. Liu, S. Xiong, X. Chu, W. Yang, Y. Peng, J. Chen, X. Cao, J. Li, Boosting the catalytic performance of CeO2 in toluene combustion via the Ce–Ce homogeneous interface, Environ. Sci. Technol. 55 (2021) 12630–12639.
[65] X. Li, J. Ma, L. Yang, G. He, C. Zhang, R. Zhang, H. He, Oxygen vacancies induced by transition metal doping in γ-MnO2 for highly efficient ozone decomposition, Environ. Sci. Technol. 52 (2018) 12685–12696.
[66] R.Q. Long, H.L. Wan, Insitu confocal microprobe Raman spectroscopy study of CeO2/BaF2 catalyst for the oxidative coupling of methane, J. Chem. Soc., Faraday Trans. 93 (1997) 355–358.
[67] J. Guzman, S. Carrettin, A. Corma, Spectroscopic evidence for the supply of reactive oxygen during CO oxidation catalyzed by gold supported on nanocrystalline CeO2, J. Am. Chem. Soc. 127 (2005) 3286–3287.
[68] Y.-J. Hao, B. Liu, L.-G. Tian, F.-T. Li, J. Ren, S.-J. Liu, Y. Liu, J. Zhao, X.-J. Wang, Synthesis of 111 facet-exposed MgO with surface oxygen vacancies for reactive oxygen species generation in the dark, ACS Appl. Mater. Interfaces 9 (2017) 12687–12693.
[69] Y. Liao, X. Zhang, R. Peng, M. Zhao, D. Ye, Catalytic properties of manganese oxide polyhedra with hollow and solid morphologies in toluene removal, Appl. Surf. Sci. 405 (2017) 20–28.
[70] J. Jia, P. Zhang, L. Chen, Catalytic decomposition of gaseous ozone over manganese dioxides with different crystal structures, Appl. Catal. B 189 (2016) 210–218.
[71] S. Guan, Q. Huang, J. Ma, W. Li, A.T. Ogunbiyi, Z. Zhou, K. Chen, Q. Zhang, HCHO removal by MnO2(x)–CeO2: influence of the synergistic effect on the catalytic activity, Ind. Eng. Chem. Res. 59 (2020) 596–608.
[72] V.P. Santos, M.F.R. Pereira, J.J.M. Órfão, J.L. Figueiredo, The role of lattice oxygen on the activity of manganese oxides towards the oxidation of volatile organic compounds, Appl. Catal. B 99 (2010) 353–363.
[73] Y.-F. Sun, J.-J. Li, F. Xie, Y. Wei, M. Yang, Ruthenium-loaded cerium dioxide nanocomposites with rich oxygen vacancies promoted the highly sensitive electrochemical detection of Hg(II), Sens. Actuators, B 320 (2020), 128355.
[74] M.E. Khan, M.M. Khan, M.H. Cho, Ce3+-ion, surface oxygen vacancy, and visible light-induced photocatalytic dye degradation and photocapacitive performance of CeO2-graphene nanostructures, Sci. Rep. 7 (2017) 5928.
[75] J. Fan, Q. Ren, S. Mo, Y. Sun, M. Fu, J. Wu, L. Chen, P. Chen, D. Ye, Transient in-situ DRIFTS investigation of catalytic oxidation of toluene over α-, γ- and β-MnO2, ChemCatChem 12 (2020) 1046–1054.
[76] P. Chen, W. Cui, H. Wang, X. Dong, J. Li, Y. Sun, Y. Zhou, Y. Zhang, F. Dong, The importance of intermediates ring-opening in preventing photocatalyst deactivation during toluene decomposition, Appl. Catal. B 272 (2020), 118977.
[77] X. Yang, X. Yu, M. Lin, X. Ma, M. Ge, Enhancement effect of acid treatment on Mn2O3 catalyst for toluene oxidation, Catal. Today 327 (2019) 254–261.
[78] J. Zhong, Y. Zeng, M. Zhang, W. Feng, D. Xiao, J. Wu, P. Chen, M. Fu, D. Ye, Toluene oxidation process and proper mechanism over Co3O4 nanotubes: Investigation through in-situ DRIFTS combined with PTR-TOF-MS and quasi in-situ XPS, Chem. Eng. J. 397 (2020), 125375.
[79] M. Ma, Q. Zhu, Z. Jiang, Y. Jian, C. Chen, Q. Liu, C. He, Achieving toluene efficient mineralization over K/α-MnO2 via oxygen vacancy modulation, J. Colloid Interface Sci. 598 (2021) 238–249.
[80] S. Mo, Q. Zhang, J. Li, Y. Sun, Q. Ren, S. Zou, Q. Zhang, J. Lu, M. Fu, D. Mo, J. Wu, H. Huang, D. Ye, Highly efficient mesoporous MnO2 catalysts for the total toluene oxidation: Oxygen-Vacancy defect engineering and involved intermediates using in situ DRIFTS, Appl. Catal. B 264 (2020), 118464.
[81] L. Long, J. Zhao, L. Yang, M. Fu, J. Wu, B. Huang, D. Ye, Room temperature catalytic ozonation of toluene over MnO2/Al2O3, Chin. J. Catal. 32 (2011) 904–916.
[82] M. Asemani, A.R. Rabbani, Detailed FTIR spectroscopy characterization of crude oil extracted asphaltenes: Curve resolve of overlapping bands, J. Petrol. Sci. Eng. 185 (2020), 106618.
[83] E.M. O'Neill, A.Z. Kawam, D.A. Van Ry, R.Z. Hinrichs, Ozonolysis of surface-adsorbed methoxyphenols: kinetics of aromatic ring cleavage vs. alkene side-chain oxidation, Atmos. Chem. Phys. 14 (2014) 47–60.
[84] Q. Li, J. Ren, Y.-J. Hao, Y.-L. Li, X.-J. Wang, Y. Liu, R. Su, F.-T. Li, Insight into reactive species-dependent photocatalytic toluene mineralization and deactivation pathways via modifying hydroxyl groups and oxygen vacancies on BiOCl, Appl. Catal. B 317 (2022), 121761.
[85] J. Mo, Y. Zhang, Q. Xu, Effect of water vapor on the by-products and decomposition rate of ppb-level toluene by photocatalytic oxidation, Appl. Catal. B 132–133 (2013) 212–218.